Material Decomposition from Photon-Counting CT using a Convolutional Neural Network and Energy-Integrating CT Training Labels

Rohan Nadkarni[a], Alex Allphin[a], Darin P. Clark[a], and Cristian T. Badea[a]
[a]Quantitative Imaging and Analysis Lab, Department of Radiology, Duke University, Durham, NC 27710, USA

ABSTRACT

Although photon counting detectors (PCD) can offer numerous benefits for CT imaging, it is difficult to generate accurate material decompositions from photon counting (PC) CT images due to spectral distortions. In this work, we present a deep learning (DL) approach for material decomposition from PCCT. To produce training and testing data for this study, we scanned 2 *ex-vivo* mice using a PCD scan protocol with a dose of 36 mGy and a multi-EID scan protocol with a dose of 296 mGy. PCD images were reconstructed using filtered backprojection. EID images were reconstructed using an iterative algorithm to reduce noise, and decomposed into iodine (I), Compton scattering (CS), and photoelectric effect (PE) material maps by a matrix inversion approach. We then trained a convolutional neural network with a 3D U-net structure using PCD images as inputs and multi-EID material maps as labels, and evaluated its performance. The 3D U-net predictions provided substantially lower RMSE compared to decomposition from PCD images using a matrix inversion approach. Measurements from iodine vials in the test set showed that 3D U-net predictions gave mean values within 0.6 mg/mL of the mean values from the multi-EID material maps and much lower standard deviation than PCD material map measurements. Our results show that the trained 3D U-net enables low-noise, quantitatively accurate material decomposition from a low dose PCD scan.

Keywords: Material decomposition, photon-counting CT, CNN, deep learning.

1. INTRODUCTION

Photon counting detectors (PCDs) offer enormous potential to improve CT imaging. A PCD counts the incident photons and bins them using energy thresholds. Each threshold image records only those photons with energy greater than a user-defined threshold. Therefore, spectral CT with a PCD can offer improved dose efficiency and spectral resolution compared to a conventional scan with an energy-integrating detector (EID) [1, 2]. Unfortunately, PCDs also suffer from effects such as K-escape, charge sharing, and pulse pileup that distort their spectral response [1]. These distortions make it difficult to perform accurate material decomposition in PCCT. Therefore, finding methods for improving material decomposition is critical to maximize the benefits of PCCT.

This work presents a method for generating low noise and accurate material decompositions from PCCT images by compensating for distortions with a convolutional neural network (CNN). Several recent works have shown great success in using deep learning (DL) for material decomposition from EID images as well as PCD images [3-6]. However, our approach differs from past work by using material decompositions derived from multi-EID CT scans as training labels. Our EID scan data is a good source for training labels because they are not affected by the spectral distortions described earlier and they have low noise due to high x-ray dose. The CNN is trained using PCCT images as inputs and material maps derived from multi-EID scans of the same specimens as labels. The trained network can then be used to generate accurate material decomposition maps from PCD images without the need to pass corresponding EID scans into the network. Our implementation and results based on micro-CT scans are presented in the following sections.

7th International Conference on Image Formation in X-Ray Computed Tomography,
edited by Joseph Webster Stayman, Proc. of SPIE Vol. 12304, 123041K
 · 0277-786X · doi: 10.1117/12.2646405

2. METHODS

2.1 Image Acquisition

All image data were acquired on our dual-source, micro-CT imaging system that has one EID (*Dexela 1512* CMOS x-ray detector with a CsI scintillator, 75 μm pixel size) and one PCD (Dectris *Santis 1604*, 150 μm pixel size, 4 energy thresholds) [7]. For this study, we scanned 2 mice that were injected with soft tissue sarcomas and liposomal-based iodine contrast agent. For both PCD and EID protocols, we acquired separate *ex-vivo* micro-CT scans for the upper and lower body.

To perform material decomposition from multi-EID micro-CT data, we acquired three different EID scans with the following parameter settings: i) 80 kVp, 40 mA, 10 ms/exposure, ii) 50 kVp, 50 mA, 16 ms/exposure, and iii) 40 kVp, 50 mA, 16 ms/exposure. Each scan used a helical trajectory, with 900 projections over 1070 degrees rotation and 1.25 cm vertical translation.

For our PCD scan, we used an X-ray tube voltage of 80 kVp, current of 2 mA, integration time of 200 ms/exposure, and energy thresholds of 25, 34, 50, and 60 keV. Just like the EID scans, this helical scan was acquired with 900 projections, 1070 degrees rotation, and 1.25 cm vertical translation. The estimated dose for this PCD scan was 36 mGy, which is much lower than the estimated dose of 296 mGy for the 3 EID scans described above.

2.2 Image Reconstruction

For the multi-EID micro-CT data, we performed an iterative reconstruction using the split Bregman method with the add-residual-back strategy [8] and rank-sparse kernel regression regularization (RSKR) [9], solving the following optimization problem:

$$\mathrm{X} = \arg\min_{X} \frac{1}{2} \sum_e || RX_e - Y_e ||_2^2 + \lambda || X ||_{BTV}.$$

Thus, we solve iteratively for the vectorized, reconstructed data, the columns of X, for each energy threshold simultaneously (indexed by *e*). The reconstruction for each threshold minimizes the reprojection error (R, system projection matrix) relative to the log-transformed projection data acquired at each threshold (the columns of Y). To reduce noise in the reconstructed results, this data fidelity term is minimized subject to the bilateral total variation (BTV) measured within and between energies via RSKR. Unlike the multi-EID data, the PCD micro-CT images were reconstructed using filtered back projection (FBP) with a Ram-Lak filter to explore the potential of our CNN to perform denoising and material decomposition simultaneously.

2.3 Material Decomposition

We performed image-based material decomposition on the EID and PCD micro-CT reconstructions using the approach of Alvarez and Macovski [10]. We chose to decompose CT images into iodine (I), Compton scattering (CS), and photoelectric effect (PE) maps. Thus, we performed a post-reconstruction spectral decomposition with I, PE and CS as bases:

$$\mathrm{X}(e) = C_{PE} M_{PE}(e) + C_{CS} M_{CS}(e) + C_I M_I(e).$$

The matrix inversion spectral decomposition was performed by solving the following linear system at each voxel:

$$\mathrm{C} = \mathrm{X}\mathrm{M}^{-1}$$

In this formulation, *C* is the least-squares solution for the concentration of I (mg/mL) and the fractions of PE and CS relative to water. *M* is a matrix of material sensitivities (attenuation/mg/mL for iodine) at each energy that was computed using vials of water and known concentrations of iodine and calcium that were included in the scans. Finally, *X* is the attenuation coefficient of the voxel under consideration at energy *e*. Orthogonal subspace projection was used to prevent negative concentrations. PCD micro-CT data was also decomposed via matrix inversion for comparison.

2.4 Animal Experiments

We used a transplant model of soft tissue sarcoma that resembles human undifferentiated pleomorphic sarcoma. A sarcoma cell line was generated from an autochthonous soft tissue sarcoma (p53/MCA model) induced in C57BL/6 wild type mice by intramuscular injection of adenovirus expressing Cas9 endonuclease and sgRNA to *Trp53* gene (Adeno-sgp53-Cas9; Viraquest) followed by intramuscular injection of the carcinogen 3-methylcholenthrene (MCA) [11]. Liposomal-based contrast agents containing iodine (Lip-I) were fabricated similar to methods described

previously [12]. Two mice with sarcomas were intravenously injected with Lip-I (1.32 mg I/kg body weight) and shortly after, were euthanized. The mice were immersed in formalin for 5 days, then scanned with our PCD micro-CT and multi-EID micro-CT. For this preliminary work, we used two mice with sarcomas, but more mice will be used in the near future.

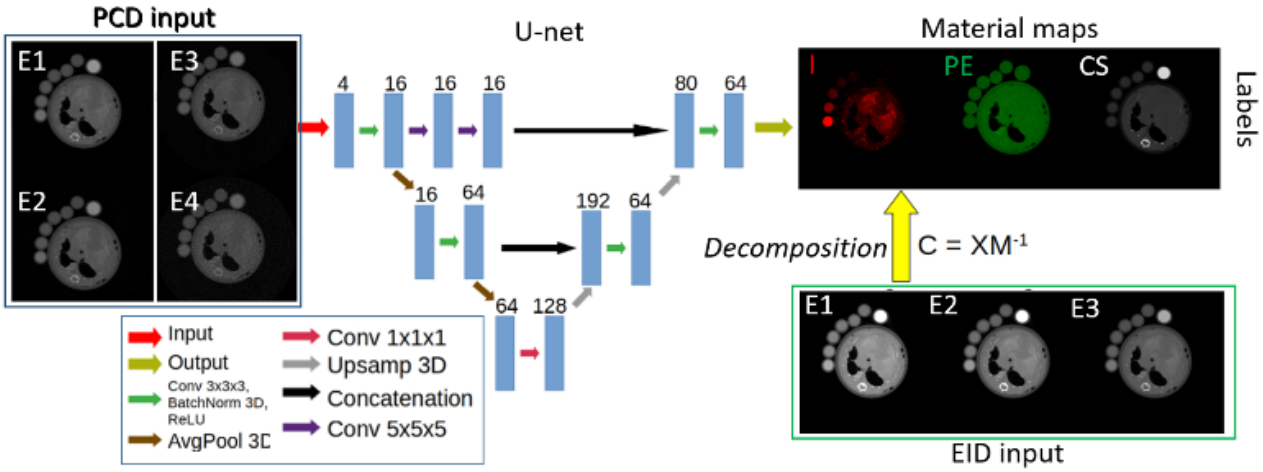

Figure 1. Diagram of our 3D U-net architecture and training procedure. The number of filters for each convolution operation is shown in the diagram. The network is trained using 3D patches of the PCD images as inputs and 3D patches of the multi-EID material maps as labels.

2.5 Network Training and Testing

Using the Pytorch library, we implemented a CNN with a 3D U-net architecture for material decomposition. The details of network architecture [13] and our training scheme are shown in Figure 1. Three matching sets of PCD and EID micro-CT scans from two mice were used for training and one set from the upper body of one mouse was held out for testing. The CNN was trained using partially overlapping 3D patches (size 38 x 62 x 62, stride 26 x 50 x 50) from PCD micro-CT images as input and smaller (size 26 x 50 x 50, stride 26 x 50 x 50), non-overlapping 3D patches of the corresponding I, CS, and PE material maps obtained via multi-EID micro-CT as labels. Each PCD energy threshold is treated as a separate input channel. Since the CNN does not use zero padding for convolutions, it crops input patches down to the size of the labels, which prevents patch artifacts when the predicted material map patches are stitched back into a complete image. The 5 x 5 x 5 convolutions ensure consistent dimensions of feature maps that are being concatenated. We trained our CNN using a mean square error (MSE) loss function with a batch size of 32, Adam optimizer [14] with learning rate of 5×10^{-5}, and 500 training epochs. Once training was complete, we used the 3D U-net to predict I, CS, and PE maps with partially overlapping 3D patches of PCD micro-CT images from the test set as inputs.

2.6 Performance Evaluation

We evaluated performance on the test set using both qualitative and quantitative methods. The material maps derived from multi-EID images via matrix inversion served as a surrogate for ground truth. For quantitative comparisons, we measured the root mean square error (RMSE) over the whole volume for PCD with matrix inversion decomposition and for 3D U-net decomposition. In addition, we compared measurements (mean and standard deviation) from I and Ca vials in the I and PE maps for all 3 decomposition approaches. For PCD with matrix inversion-based decomposition, we used the FBP reconstruction as the input because this is also what the 3D U- net takes as an input. Finally, we generated modulation transfer functions (MTF) derived from iodine maps for the EID decomposition and the 3D U-net decomposition to assess how well the CNN preserves spatial resolution.

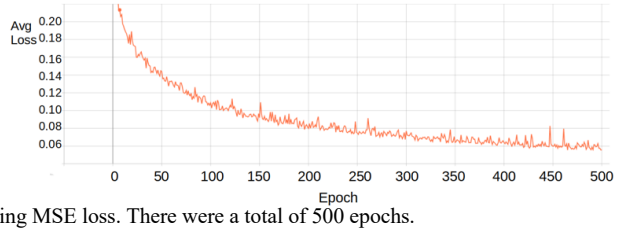

Figure 2. Average training MSE loss. There were a total of 500 epochs.

3. RESULTS

The training loss curve (Figure 2) indicates a decrease in error over the 500 epochs. An axial slice with decompositions provided by the multi-EID data, the PCD micro-CT via matrix inversion and the predictions from 3D U-net are shown in Figure 3. Although the CNN results are the closest to the multi-EID, some smoothing is also noticeable. The 3D U-net prediction appears superior to the PCD decomposition via matrix inversion, which shows higher levels of noise.

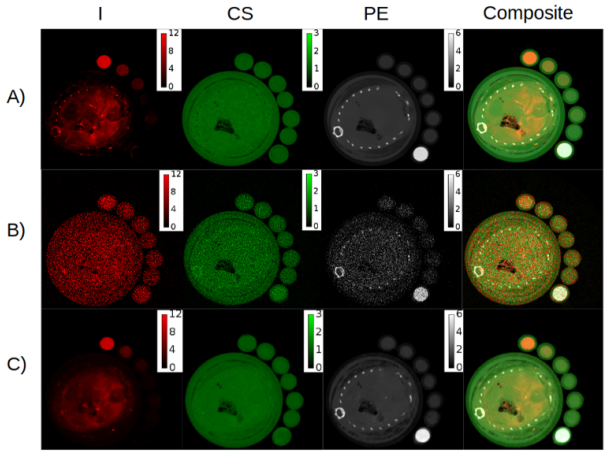

Figure 3. I, CS, PE, and composite material maps in an axial slice from the test set for A) decomposition using matrix inversion from multi-EID scans B) decomposition using matrix inversion from the PCD scan and C) decomposition via prediction by the 3D U-net.

Figure 4 shows the RMSE of I, CS and PE material maps for both the 3D U-net prediction and the standard PCD decomposition via matrix inversion. The largest error in the standard PCD decomposition is for the I map. Using the trained 3D U-net reduced the RMSE by 2.597 mg/mL in the I map, 0.221 in the CS map, and 0.370 in the PE map. Note that the expected CS and PE values in water were normalized to 1.0 for the EID data.

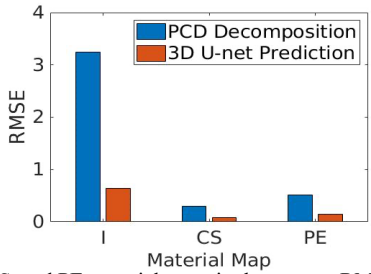

Figure 4. RMSE of I, CS, and PE material maps in the test set. RMSE values for both PCD decomposition via matrix inversion and 3D U-net predicted decomposition are computed relative to the multi-EID decomposition via matrix inversion.

Quantitative measurements from I and Ca vials included in the test set scans are shown in Figure 5. Compared to multi-EID decomposition, the PCD decomposition via matrix inversion shows mean measurements that overestimate I concentrations and underestimate PE values in the Ca vial. The measurements from 3D U-net prediction are more accurate since they are much closer to the multi-EID ground truth. The mean value from the 3D U-net predicted material map is within 0.6 mg/mL of the mean value from the multi-EID material map for both iodine vials. Measurements from the 3D U-net prediction consistently provide better precision as indicated by smaller standard deviation than measurements from PCD decomposition via matrix inversion. This result is consistent with the previous observation of reduced noise from 3D U-net decomposition.

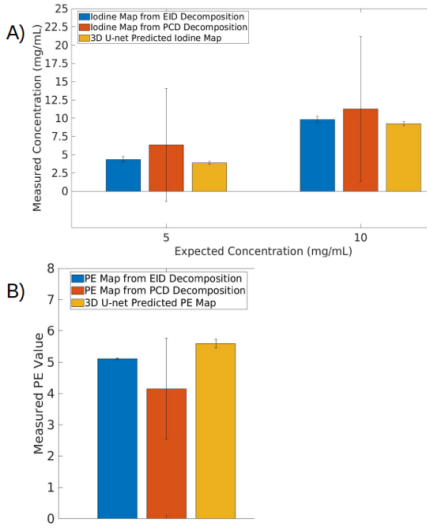

Figure 5. Mean and standard deviation of intensity values measured in vials of known concentration from multi-EID decomposition, PCD decomposition, and 3D U-net predicted material maps. A) Measurements in I map from I vials, with the expected concentrations shown on the x-axis. B) Measurements in PE map from a vial with 50 mg/mL of calcium in water.

Figure 6 shows an axial slice from the absolute difference maps between 3D U-net prediction and multi-EID decomposition for each material. These maps indicate that the 3D U-net predictions tend to have the greatest error at edges and in highly enhancing structures such as the bone.

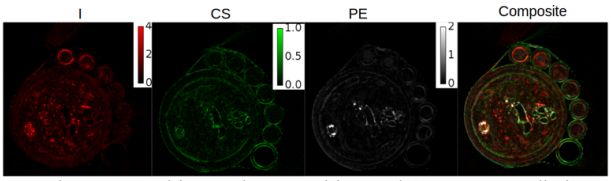

Figure 6. Absolute difference between multi-EID decomposition and 3D U-net prediction material maps in an example axial slice from the test set.

The MTFs for the multi-EID decompositions and 3D U-net predictions are in Figure 7. At 10% MTF, the prediction from 3D U-net has a spatial resolution of 257.5 μm, while the multi-EID decomposition has a spatial resolution of 231.5 μm. This confirms the blurring added by the CNN decomposition, and is consistent with the edge errors observed in the absolute difference maps from Figure 6.

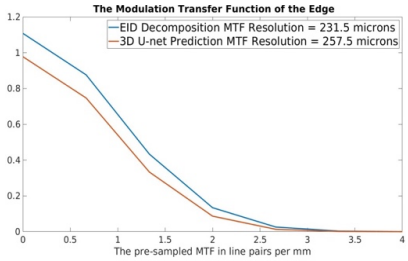

Figure 7. MTF from multi-EID decomposition and from 3D U-net prediction.

4. CONCLUSIONS

In this work, we implemented a unique approach for DL material decomposition from PCD images by using multi-EID material maps as training labels. Our results on the test set show that a 3D U-net trained with this method can perform material decomposition from a PCD scan with greater quantitative accuracy and precision than the conventional matrix inversion-based approach. There are a few limitations that merit further discussion. The material maps predicted by the 3D U-net produced overly smooth images, resulting in errors at edges. It is possible that these errors can be mitigated by implementing a more sophisticated loss function than MSE such as gradient correlation loss [15]. In addition, like other DL approaches, our trained CNN can only be used on PCD images with similar scan and reconstruction protocols to the training data. Despite these issues, our CNN-based approach is a powerful method for compensating for spectral distortion during material decomposition and exploiting the improved dose efficiency offered by PCCT imaging.

REFERENCES

[1] K. Taguchi and J. S. Iwanczyk, "Vision 20/20: Single photon counting x-ray detectors in medical imaging," *Med Phys,* vol. 40, no. 10, p. 100901, Oct 2013.

[2] M. J. Willemink, M. Persson, A. Pourmorteza, N. J. Pelc, and D. Fleischmann, "Photon-counting CT: Technical Principles and Clinical Prospects," *Radiology,* vol. 289, no. 2, pp. 293-312, Nov 2018.

[3] J. F. P. J. Abascal, N. Ducros, and V. Pronina, "Material Decomposition in Spectral CT Using Deep Learning: A Sim2Real Transfer Approach," *IEEE Access,* vol. 9, Special Section on Multi-Energy Computed Tomography and its Applications, pp. 25632-25647, 2021.

[4] D. P. Clark, M. Holbrook, and C. T. Badea, "Multi-energy CT decomposition using convolutional neural networks," presented at the SPIE Medical Imaging, 2018.

[5] H. Gong, S. Tao, K. Rajendran, W. Zhou, C. H. McCollough, and S. Leng, "Deep-learning-based direct inversion for material decomposition," *Med Phys,* vol. 47, no. 12, pp. 6294-6309, Dec 2020.

[6] W. Zhang *et al.*, "Image domain dual material decomposition for dual-energy CT using butterfly network," *Med Phys,* vol. 46, no. 5, pp. 2037-2051, May 2019.

[7] M. D. Holbrook, D. P. Clark, and C. T. Badea, "Dual source hybrid spectral micro-CT using an energy-integrating and a photon-counting detector," *Phys Med Biol,* vol. 65, no. 20, 2020.

[8] H. Gao, H. Yu, S. Osher, and G. Wang, "Multi-energy CT based on a prior rank, intensity and sparsity model (PRISM)," *Inverse Probl,* vol. 27, no. 11, p. 115012, Nov 1 2011.

[9] D. P. Clark and C. T. Badea, "Hybrid spectral CT reconstruction," *PLOS ONE,* vol. 12, no. 7, p. e0180324, 2017.

[10] R. E. Alvarez and A. Macovski, "Energy-selective reconstructions in X-ray computerized tomography," *Phys Med Biol,* vol. 21, no. 5, pp. 733-44, Sep 1976.

[11] A. J. Wisdom *et al.*, "Single cell analysis reveals distinct immune landscapes in transplant and primary sarcomas that determine response or resistance to immunotherapy," *Nat Commun,* vol. 11, no. 1, p. 6410, Dec 17 2020.

[12] S. Mukundan, Jr. *et al.*, "A liposomal nanoscale contrast agent for preclinical CT in mice," *AJR Am J Roentgenol,* vol. 186, no. 2, pp. 300-7, Feb 2006.

[13] O. Ronneberger, P. Fischer, and T. Brox, "U-Net: Convolutional Networks for Biomedical Image Segmentation," Cham, 2015: Springer International Publishing, in Medical Image Computing and Computer-Assisted Intervention – MICCAI 2015, pp. 234-241.

[14] D. P. Kingma and J. L. Ba, "Adam: A Method for Stochastic Optimization," *International Conference on Learning Representations,* 12/22 2014.
[15] D. P. C. M. D. Holbrook, C. T. Badea " Deep learning based spectral distortion correction and decomposition for photon counting CT using calibration provided by an energy integrated detector " *SPIE Medical Imaging,* vol. 11595, 15 February 2021 2021.